Overview of the TCV Tokamak Program: Scientific Progress and Facility Upgrades

S. Coda for the TCV team[1] and the EUROfusion MST1 team[2]

Ecole Polytechnique Fédérale de Lausanne (EPFL), Swiss Plasma Center, CH-1015 Lausanne, Switzerland

E-mail contact of main author: stefano.coda@epfl.ch

Abstract. The TCV tokamak is augmenting its unique historical capabilities (strong shaping, strong electron heating) with ion heating, additional electron heating compatible with high densities, and variable divertor geometry, in a multifaceted upgrade program designed to broaden its operational range without sacrificing its fundamental flexibility. The TCV program is rooted in a three-pronged approach aimed at ITER support, explorations towards DEMO, and fundamental research. A 1-MW, tangential neutral beam injector (NBI) was recently installed and promptly extended the TCV parameter range, with record ion temperatures and toroidal rotation velocities and measurable neutral-beam current drive. ITER-relevant scenario development has received particular attention, with strategies aimed at maximizing performance through optimized discharge trajectories to avoid MHD instabilities, such as peeling-ballooning and neoclassical tearing modes. Experiments on exhaust physics have focused particularly on detachment, a necessary step to a DEMO reactor, in a comprehensive set of conventional and advanced divertor concepts; a surprising independence of detachment threshold density on flux expansion was revealed when the ion ∇B drift pointed away from the X-point. Fundamental investigations of the power decay length in the scrape-off layer (SOL) are progressing apace, again in widely varying configurations and in both D and He plasmas; in particular, the double decay length in L-mode limited plasmas was found to be replaced by a single length at high SOL resistivity. Experiments on disruption mitigation by massive gas injection and electron-cyclotron resonance heating (ECRH) have begun in earnest, in parallel with studies of runaway electron generation and control, in both stable and disruptive conditions; a quiescent runaway beam carrying the entire electrical current appears to develop in some cases. Developments in plasma control have benefited from progress in individual controller design and have evolved steadily towards controller integration, mostly within an environment supervised by a tokamak profile control simulator. TCV has demonstrated effective wall conditioning with ECRH in He in support of JT-60SA operation.

1. Introduction

The Tokamak à Configuration Variable (TCV) [1] is one of three national tokamak devices operating as European facilities within the Medium-Size Tokamak (MST) Task Force of the EUROfusion consortium [2]. It also runs as the flagship national nuclear-fusion facility of the Swiss Plasma Center (SPC) – formerly Centre de Recherches en Physique des Plasmas (CRPP). Fully embedded within an institution of higher learning, the Federal Institute of Technology in Lausanne (EPFL), TCV at once provides a training ground for students, both at the graduate and undergraduate levels, and relies on the same young human potential to assist the senior staff in the intensive operation of the device and the continuous development and maintenance of diagnostics and other subsystems.

TCV features a major radius of 0.88 m, a minor radius of 0.25 m, a vacuum toroidal field up to 1.5 T, and plasma current up to 1 MA. It has long been defined by its strong versatility in plasma shaping, made possible by 16 independently-powered poloidal-field coils, supplemented by 2 internal coils to stem axisymmetric instabilities with high growth rate. This has motivated the allotment of a significant fraction of its recent experimental program to a determined search for alternative and unconventional configurations in view of meeting the DEMO challenges. More conventional ITER-relevant scenarios occupy nevertheless an equally important fraction, particularly since the historically dominant Electron Cyclotron Resonance Heating (ECRH) was augmented by Neutral Beam Heating (NBH) [3]. Experimental time is also always reserved for more fundamental or speculative investigations,

[1] see Appendix

[2] see appendix of H. Meyer et al (OV/P-12) Proc. 26th IAEA Fusion Energy Conf. 2016, Kyoto, Japan

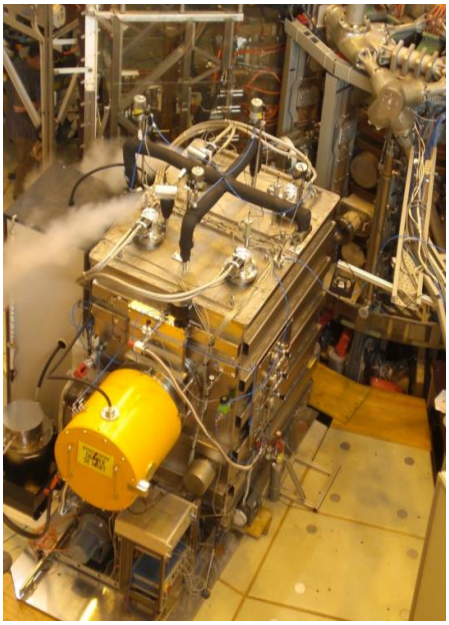

FIG. 1. The neutral beam injector of TCV.

often motivated by contemporary theoretical developments and predictions.

This paper reports on scientific results primarily from the 2015-2016 campaign, which followed a nearly 2-year shutdown for NBH installation and other upgrades and was dominated by the EUROfusion contribution, and on the phased facility upgrade underway [4]. Many of the experiments described in this paper also had counterparts in the other operating MST facility, ASDEX Upgrade (AUG) [2]. Section 2 discusses the commissioning of and first results with NBH, and the remaining upgrades; section 3 reports on ITER-related scenario development; section 4 is on exhaust physics and detachment, including advanced divertor configurations; section 5 deals with disruptions and runaway electron physics; section 6 relates developments in real-time control; impurity dynamics and wall cleaning experiments are described in section 7, followed by conclusions and an outlook in section 8.

2. NBI commissioning and further facility upgrades

A 1-MW, 15-25 keV neutral-beam injector (NBI) has been installed on TCV in 2015 (Fig. 1), connected to an oblique midplane port that defines a trajectory not intersecting the central column, thus enabling a double pass through the plasma cross section for enhanced absorption, in the co- or counter-current direction [3]. The positive-ion-source based injector can operate for 2 s with either deuterium or hydrogen, with a full-energy fraction of 75%. To accommodate the (elliptical) beam size the vacuum vessel was endowed with a new opening and 17×22 cm port; this in fact was replicated at a second location in view of a future second injector. The facility was shut down from November 2013 to June 2015 for this in-vessel work and the infrastructure modifications to prepare for the injector installation. Beam operation commenced in January 2016 and continued with high reliability during the ensuing campaign, with over 580 shots fired into TCV plasmas. Vessel protection is ensured by pyrometers observing the graphite beam dump, the inner wall, and the beam duct opening, interlocked to the NBI power supply; additional protection is provided by interlocks based on plasma-density and thermocouple measurements. Overheating of the vessel has not been an issue. However, a non-optimal beam profile has caused overheating of the beam duct, necessitating the addition of active water cooling and a temporary operational limitation of 0.5 MJ injected energy per shot from the available ~2 MJ. Tuning of the ion optics is currently underway with the goal of relaxing this limitation, in conjunction with enhanced duct cooling [5,6].

With NBH, central (carbon) ion temperatures in excess of 2.5 keV and toroidal rotation velocities of 250 km/s have been obtained, both well above any previous TCV values (<1 keV and 30 km/s intrinsic rotation) [6]. Initial experiments were carried out to compare on-axis and off-axis co-injected NBH with the aid of modeling with NUBEAM (Monte Carlo fast-ion module) and TRANSP (transport analysis code) [7]. Off-axis NBH is achieved in TCV by shifting the plasma vertically. Counter-ECCD was employed to avoid sawtooth crashes, which would complicate the comparison. Fairly high losses in the beam duct (~10%), from shine-through (~20%), and from loss orbits (~10%) have to be assumed for NUBEAM to produce fast-ion densities consistent with measurements; an alternative explanation –

undiagnosed thus far – could be provided by anomalous turbulent fast-ion losses or by the effect of beta-induced Alfvén eigenmodes (BAE), a possible signature of which is detected in magnetic spectrograms.

A loop voltage drop is clearly detected at the NBH onset, demonstrating net current drive from beam ions. Furthermore, a clear difference in β and in loop voltage is observed between the on- and off-axis cases, and the absolute values are well reproduced by TRANSP when the ion confinement time is set to 5 ms (Fig. 2), corresponding to a high neutral density of 2×10^{16} m^{-3} at the plasma boundary, consistent with absolutely calibrated Neutral Particle Analyzer measurements. Preliminary agreement is seen under these conditions between the Fast-Ion D-Alpha (FIDA) emission predicted by the FIDASIM module and measurements both of active radiation (by a vertically viewing system intersecting the beam) and passive radiation with a toroidally viewing apparatus [7].

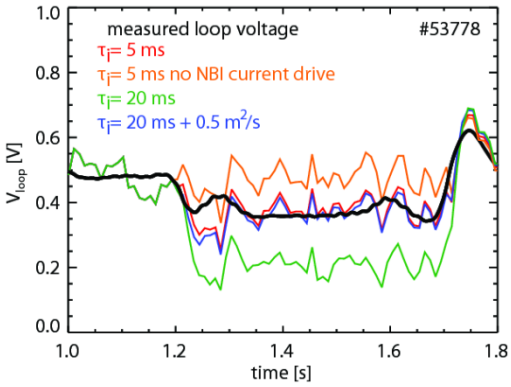

FIG. 2. Measured loop voltage vs value predicted by TRANSP with different ion confinement time values, also in a case with suppressed NBCD and a case with ad-hoc turbulent diffusion. (Reproduced from [7].)

Co- and counter-injection have also been compared for both on- and off-axis heating, with qualitatively consistent resulting trends for β and loop voltage, to be analyzed with TRANSP modeling. Magnetic-turbulence data have been collected in these experiments with a set of newly installed, fast, 3D, Low Temperature Co-fired Ceramic (LTCC) magnetic probes [8] in view of studying the role of turbulence in fast-ion confinement.

The NBH installation was the first step in a wide-reaching, phased sequence of upgrades [9]. A new 750-kW, 82.7-GHz gyrotron has also been commissioned, adding to three remaining first-generation sources to provide a total 2.25-MW second-harmonic X-mode (X2) ECRH power. A second 750-kW source is also presently in the final commissioning phase. In 2018-2019, two 1-MW dual-frequency (X2 and X3) gyrotrons and a second, oppositely injected, higher-energy (50-60 keV) 1-MW neutral beam will be commissioned. Finally, a substantial modification of the vacuum chamber itself is being actively planned for the 2019-2020 horizon, to introduce variable-configuration baffles with the goal of investigating the effect of variable divertor closure on exhaust and plasma performance, particularly in advanced-divertor configurations. This may be accompanied by cryopumping and by the addition of supplementary divertor coils. The physics understanding and modeling validation capabilities this upgrade can bring are a vital necessity for a credible assessment of the viability of alternate configurations for a fusion power plant [4].

3. Scenario development

In the quest to achieve the high confinement required for the target Q=10 fusion energy gain in ITER, it is imperative to maximize the pedestal height compatibly with the requirements of peeling-ballooning stability. A significant limitation may be imposed by insufficiently low collisionality dictated e.g. by constraints related to the metal plasma facing components. This in turn reduces the edge bootstrap current away from the optimum value for maximum pedestal pressure. Theory suggests that a stable path may nevertheless be charted to the target pressure at reduced edge current by approaching it from above, i.e., by increasing the plasma pressure in L-mode, before the transition to H-mode. A joint experiment was successfully performed on MAST, JET, and TCV to test this hypothesis [10]. The key element in the experimental strategy was initial L-mode operation in a magnetic configuration especially

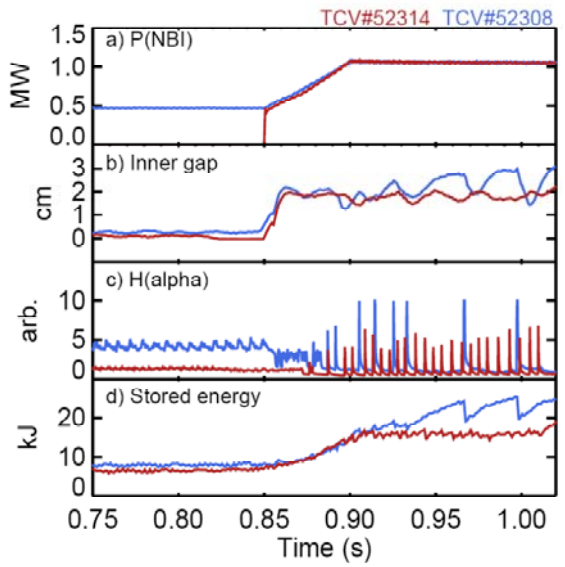

FIG. 3. (a) NBH power, (b) inner gap, (c) H_α emission, (d) stored energy in two shots with and without L-mode pre-heating. (Reproduced from [10].)

adverse to the L-H transition. In TCV this takes the form of a single-null topology with unfavorable ion ∇B drift and a small (1 cm) wall gap. Once the core pressure and the pedestal height reach saturation with the available power, the other X-point is activated and the wall gap is quickly increased to 2 cm, triggering the L-H transition. The ballooning stabilization results in a lower ELM frequency, which in turn acts to increase the pedestal pressure further: a higher stored energy – by up to 50% – is then observed to last through several ELM cycles (Fig. 3). A predictive model framework incorporating the EUROPED pedestal model in the JINTRAC integrated modeling code, while succeeding for a metal-wall machine (JET), substantially underestimates the pedestal height in the MAST and TCV carbon-wall devices [10]. Remaining challenges for this strategy are the sustainment of the high performance for several confinement times and the tailoring of the discharge to both limit the ELM heat loads to tolerable values and to achieve satisfactory impurity control.

The stability of neoclassical tearing modes (NTMs) remains an important issue for ITER, because of the loss of confinement or wholesale control they can engender. "Triggerless" destabilization, in the absence of seed islands driven by sawtooth crashes, is a particular concern. Central co-ECCD in low-rotation TCV plasmas can modify the rotation profile, reversing the average flow direction from counter- to co-current, and can excite both (3,2) and (2,1) NTMs without apparent triggers. The destabilization appears to be due to modification of the q profile by ECCD and an increase in Δ' [11]. Recent work has focused on understanding the mechanisms for the induced rotation. The effect of ECCD was modeled assuming three torque sources with increasingly long time scales: a direct torque associated with the displacement current, a torque related to the turbulent Reynolds stress, and a torque from density pump-out and modifications in edge recycling. A good match with experimental data is obtained when the Reynolds stress is the dominant effect [12].

Other experiments were also explicitly designed to exploit the inherent stepladder scaling approach of the MST concept, with twin versions on AUG and TCV [2]. The mechanisms by which sawtooth cycles expel angular momentum and impurities were investigated with the AUG shape reproduced identically in TCV and similarly low collisionality and edge safety factor (the primary different dimensionless parameter being ρ*). Scenarios with negative core q shear and internal transport barriers were revisited with NBH to explore paths towards and above the no-wall MHD limit. H-mode operation with high confinement in the proximity of the density limit was also explored in parallel with AUG. All this is work in progress.

Following earlier experiments demonstrating a strong improvement in L-mode confinement [13] as well as an increase in H-mode ELM frequency with negative triangularity [14], new experiments were performed during the MST campaign to study the overall H-mode confinement and pedestal characteristics for varying triangularity. Data analysis is underway.

TCV contributed data to a multi-device database of discharge terminations, assembled to provide specifications for the controlled shutdown of ITER plasmas [15].

4. Exhaust physics and detachment in conventional and innovative configurations

Investigations into the physics of plasma exhaust and detachment have been conducted over multiple fronts, in recognition of the paramount importance of the issue for the safe operation of a future fusion reactor. The mechanics of detachment have been studied primarily through density ramps and with N2 seeding to control edge radiation, in a wide variety of divertor configurations ranging from the conventional single-null (SN) – with varying poloidal or total flux expansion – through the family of snowflake topologies to advanced solutions such as the super-X and X-point-target divertors [16]. Several experiments have explored fundamental questions on heat load and scrape-off-layer (SOL) properties in L- and H-mode, again exploiting the extensive plasma shape and topology variations afforded by the TCV control equipment.

All these experiments have benefited from an extensive array of diagnostics, including a vertical and a horizontal infrared (IR) camera (the latter being movable between two vertical positions) ensuring broad coverage of the floor and of the inner wall, 114 wall-mounted Langmuir probes (LPs), a fast reciprocating probe (RP – on loan from UCSD) [17], tomographic sets of foil and AXUV bolometers, a fast framing visible camera, a four-camera set with identical optics and viewline and different spectroscopic filters, and a visible-light divertor spectroscopy system (DSS). The latter was a recent addition that benefited particularly from advancements in Balmer series analysis techniques [18].

All the detachment experiments were performed in Ohmic L-mode plasmas in reverse field, i.e., with the ion ∇B drift directed away from the X-point in the standard lower-null configuration, which is known to facilitate detachment and increases the operational range for L-mode. In a density ramp, detachment is identified by saturation and roll-over of the ion flux to the outer target, with most of the reduction occurring near the strike point [16]. The inner target on the central wall, characterized by a much shorter connection length, remains attached in these experiments. Before the onset of detachment, at ~70% of the detachment density, the C III and D_α radiation fronts separate from the target and move towards the X-point, as a result of the temperature reduction engendered by the density increase, and eventually peak at the X-point (Fig. 4), though substantial radiation subsists from the outer leg at the roll-over time [19]. After the onset of detachment, a gradual broadening or "shoulder" is generally seen by the RP to form in the upstream SOL density profile. The C III front then remains stationary and density can be increased further until a disruptive density limit is reached. In contrast with the C III emission, the recombination front is inferred by DSS measurements never to stray more than a few cm from the target, unlike what is observed generally in higher-density tokamaks [16]. The longer mean free path for ionization and the open divertor of TCV may be responsible for this variance.

In the conventional SN scenario, the detachment dynamics appear to be broadly unaffected by variations in fueling and wall gap. During the density ramp, the radiated power increases along with the Ohmic power, such that the power exhausted through the divertor is approximately constant. Detachment is stronger and more decisive at higher (340 kA) than lower (250 kA) plasma current. Around the roll-over time, the radiated power from the inner SOL and outer leg saturates and in

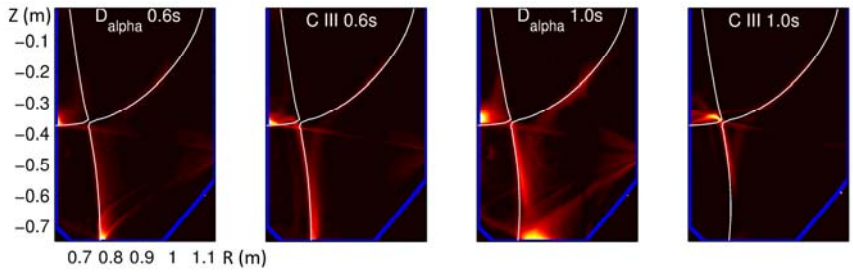

FIG. 4. D_α and C III emissivity profiles 0.4 s before and at the onset of detachment (occurring at 1.0 s). (Reproduced from [19].)

particular on the outer leg the emission profile narrows around the X-point; radiation from the outer SOL however increases [19]. Signs of hysteresis are detected, particularly in the C III emission, when a density ramp-down is effected following detachment. The interpretive OSM-EIRENE/DIVIMP suite of codes was employed to verify the consistency of experimental measurements before and after detachment: with input data from Thomson scattering, LPs, DSS, and C III imaging, the simulation generates predictions for other measurements, particularly the D_γ/D_α ratio. The agreement is found to be fairly satisfactory [19].

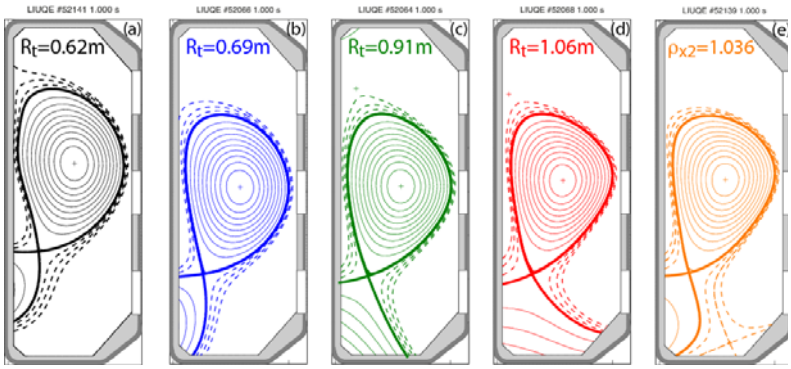

FIG. 5. Flux-surface contours of TCV equilibria for (a-d) varying major radius of the outer strike point, up to the super-X case, (e) X-point-target divertor. (Adapted from [20].)

Poloidal flux expansion (varied in TCV by over a factor 4) automatically increases the wetted area, the connection length, the divertor volume, and the divertor leg width. No change in detachment threshold, however, is detected during the flux variation, although the ion flux decrease during the roll-over phase is larger at high flux expansion [16,20]. This is contrary to expectations based on the standard two-point model. Similar observations are made in the case of an increase in flux-surface *flaring* near the target, a variant of this concept termed X divertor. A variation of the connection length can also be obtained in TCV without attendant changes in flux by varying the vertical plasma position: the threshold density is found to decrease and the depth of detachment (ion flux drop) to increase with increasing leg length.

More advanced manipulations of the divertor topology may be required in a DEMO reactor facility (Fig. 5). In the super-X divertor, total flux expansion is achieved by moving the target to a larger major radius. In this case, a decrease in parallel heat flux is also expected from the magnetic-field gradient along the leg, and this is in turn expected to facilitate detachment. While the heat flux reduction is confirmed experimentally in TCV, neither an increase in target density nor a decrease of the detachment threshold density is observed [16,20].

The snowflake (SF) divertor, characterized by two closely spaced X-points, has been extensively studied on TCV, in the two known variants defined by whether the secondary X-point is in the private (SF+) or common (SF-) flux region, the latter case further categorized as high-field-side (HFS) or low-field-side (LFS) SF- depending on the secondary X-point location [21,22]. As meaningful connection-length increase can be achieved in TCV only in the SF- case, detachment experiments focused on the LFS SF-. In this case both primary strike points are on the inner wall: detachment at the lower point nevertheless occurs at similar densities as in the SN case, and with a stronger ion flux drop; detachment at the outermost secondary strike point begins simultaneously but remains shallow except at very small X-point separation values (Fig. 6) [16]. Nitrogen seeding was applied to this scenario to test the specific prediction by EMC3-EIRENE of an enhanced impurity radiation region between the two X-points [23], which was indeed confirmed. The X-point-target divertor (Fig. 5) – also realized in TCV – is topologically akin to the LFS SF-, with the secondary X-point close to the target; obviously increasing the connection length, this configuration nevertheless exhibits similar detachment dynamics to the standard SN case [16,20].

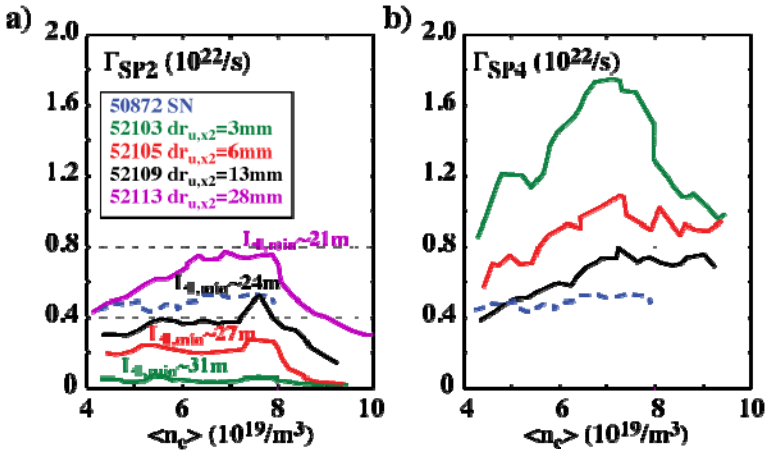

FIG. 6. Ion currents to (a) SP2 (lower primary inner-wall strike point) and (b) SP4 (outermost secondary strike point) for density ramps in LFS SF- configurations for varying X-point separation $dr_{u,x2}$. (Reproduced from [16].)

The insensitivity of the detachment threshold to flux expansion in reverse field constitutes a very distinct surprise. It is speculated that convective heat flux components and the varying dynamics of neutrals, not considered in the two-point model, could hold a key to this puzzle.

The fundamental properties of the SOL and radial transport within it are key to controlling the heat load on plasma-facing wall components. A systematic study was undertaken on TCV in the standard SN configuration in both D and He plasmas with the explicit aim of contributing to a multi-device database on the scaling of the upstream-remapped power decay length, λ_q, and spreading factor, *S*, primarily on varying divertor leg length (via a vertical shift of the plasma) [24]. While λ_q is found to increase with the leg length, no clear trend is detected for *S* [25]. The hypothesis that λ_q is determined by upstream transport features and is unaffected by plasma and divertor geometry was tested by comparing TCV data with a simple Monte Carlo model of SOL transport (MONALISA). The hypothesis is strongly put into question by the results, which indicate that transport and divertor geometry cannot be easily disentangled [24].

The in-out λ_q asymmetry observed earlier in AUG [26] was also explored, with varying upper triangularity (from positive to negative), varying field direction and both D and He as main plasma species. SOL transport was investigated in parallel both in L- and H-mode in the SF topology. This dataset is currently under analysis.

In the limited L-mode regime, through which all tokamak discharges pass during the startup phase at relatively low density, it is well established that the heat flux profile is inadequately described by a single λ_q, but well described instead by two scale lengths, with a steeper decay in the near SOL [27]. The resulting enhanced heat deposition on the limiter has motivated a redesign of the ITER first wall panel. New experiments on TCV (in both D and He) have determined for the first time that the narrow feature disappears at low plasma current or high density (Fig. 7), coincident with the normalized resistivity increase taking the near SOL from the sheath-limited to the conduction-limited regime (ITER is however expected to be in the former regime) [28]. A correlation of the narrow feature with the appearance of non-ambipolar currents (measured by LPs) was established, even though their associated heat flux cannot directly explain the effect. E×B shear has also been proposed as a possible mechanism, but this remains to be tested. The first nonlinear simulations with the Braginskii solver GBS have been performed for TCV and reproduce well the double scale length, although they underestimate the near-SOL heat flux component; the disappearance of the narrow feature at high resistivity is also not seen in the simulation on the limiter side [29].

The SOL density profile broadening discussed earlier for high-density conditions is in fact observed also in the absence of detachment in forward field (with ion ∇B drift towards the X-point). It has been suggested that its cause could be enhanced cross-field convective (filamentary or blob-like) transport overtaking the parallel losses [30]. The TCV capabilities for flux expansion were employed for a scan of the parallel connection length to investigate

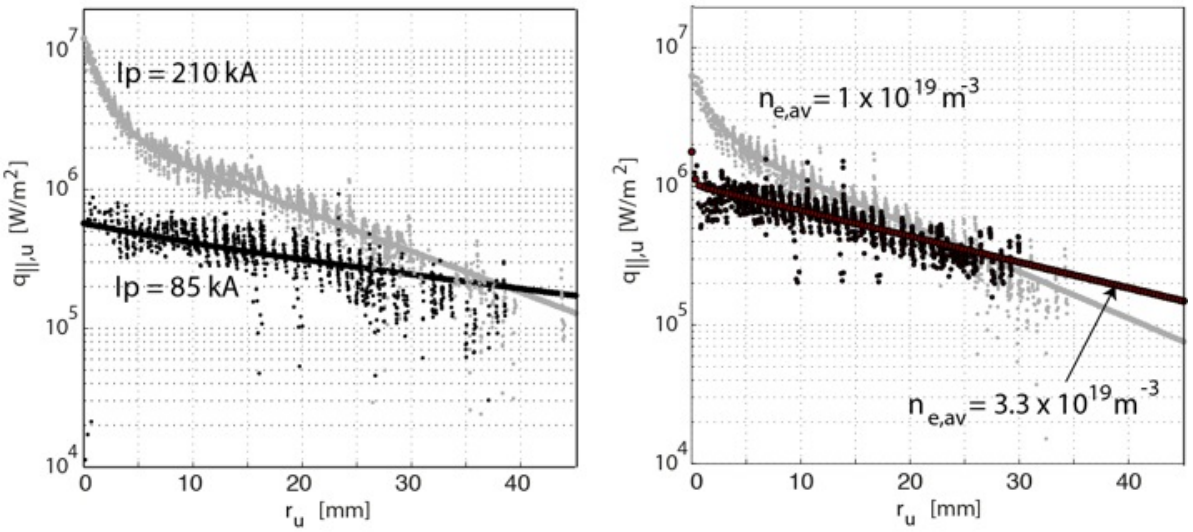

FIG. 7. Profiles of parallel heat flux to the target mapped to the outboard midplane for inboard limited plasmas for (left) two current values at line-averaged density 1.7×10^{19} m^{-3} and (right) two density values at a plasma current of 140 kA. (Reproduced from [28].)

the blob dynamics in both D and He; additionally, plasma current scans were performed (shoulder formation being more pronounced at low current) as well as a comparison between the lower and upper single-null and double-null topologies [31]. Overall, the density broadening correlates statistically with larger blob size (as determined from RP data); however, no direct dependence is evinced on the connection length, which varied by a factor 2 in these scans [31]. Thus, while this work corroborates turbulence playing a role in the shoulder development, the precise physical mechanisms at play remain to be understood.
Dedicated experiments to study heat loads from type-I ELMs were carried out for the first time on TCV in neutral-beam-heated H-modes, confirming the usual asymmetry between inner and outer targets. A quantitative analysis, relying strongly on infrared measurements, is underway.

5. Physics of disruptions and runaway electrons

The connected areas of disruptions and runaway electron physics have not been at the forefront of TCV research in the past. This has now changed, with a significant thrust in the last campaign that will certainly continue as disruption mitigation is a top objective of the MST program in particular.
A study of the disruptive density limit as a fraction of the Greenwald density has found it to increase with edge safety factor and with triangularity (δ), such that the Greenwald limit can be achieved on TCV at low current (q_{95}~6) and positive δ [29]. These results mirror a similar study on T-10. A suppression of the sawtooth cycle, accompanied by a loss of confinement, is generally found to precede the disruption, with a macroscopic evolution that has been hypothesized to constitute a slow-growing thermal instability. The database assembled on TCV shows however that at ITER values of q_{95} and δ this suppression does not occur [32].
An external fast injection valve, primarily conceived for trace impurity transport studies, has been effectively employed as a disruption mitigation valve by a large increase of the back pressure to effect massive gas injection (MGI). Preliminary disruption mitigation experiments have been performed on TCV with promising results, proving their feasibility [33].
Conversely, noble gas puffing has been used to *induce* disruptions. In particular, in a study on disruption mitigation by ECRH, neon injection was employed in a low-density type-I ELMy H-mode to initiate the disruption. A radiation threshold was used to trigger the ECRH power,

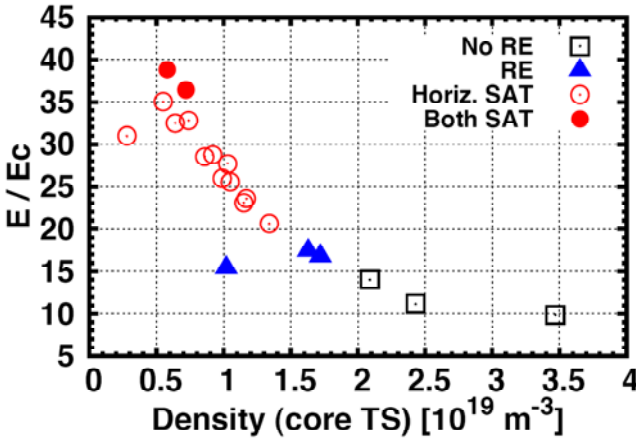

FIG. 8. Classification of runaway-electron discharges vs central density and normalized toroidal electric field, based on signals from heavily shielded HXR detectors: no RE = no signal, RE = finite signal, Horiz. SAT = midplane detector saturated, Both SAT = midplane and top detectors saturated. (Reproduced from [36].)

directed near the q=2 surface in co-ECCD mode. A scan of the deposition location reveals a narrow optimum at q=2 and an actual acceleration of the disruption for slightly smaller minor radius, consistent with earlier results from FTU and AUG [34].

Runaway electron (RE) experiments were performed in circular Ohmic L-mode plasmas. Heavily shielded hard X-ray (HXR) detectors constitute the main diagnostic tool [35]. A stationary RE beam is generated in the quiescent, non-disruptive phase when the line-averaged density lies below 3×10^{19} m^{-3} and the toroidal electric field normalized to the critical field exceeds 15 (Fig. 8) [36]. Hysteresis in RE generation and suppression (by successive density ramp-down and ramp-up) is observed only when sawteeth are not present: it is conjectured that sawteeth expel REs efficiently so that the RE population is "reset" at each crash. Runaway mitigation was attempted with only partial success: Ne and Ar injection leads to increased dissipation but not to total suppression, arguably because of insufficient throughput [36].

Disruptions were also initiated by Ne or Ar MGI to study the associated RE beam formation. Robust, reproducible RE beams are generated with pre-disruption line-averaged densities below 2.5×10^{18} m^{-3}. Gas injection at the top level of the plasma cross section is, counter-intuitively, found to be more effective than on the midplane, where the valve is closest to the plasma. Full current replacement by REs can be obtained, yielding seemingly pure RE-beam discharges lasting up to 650 ms, as evidenced by the vanishingly low bulk electron temperature (<20 eV) and current decay time – at zero applied loop voltage – much longer than the L/R time of the bulk. A pre-existing population of fast electrons, signaled by a loop voltage drop and rise in HXR signal, appears key to this scenario. Once the RE beam is generated, it can generally be stably controlled in various ways, e.g., shifted vertically or ramped in current at varying rates using the Ohmic transformer, down to ~20 kA [36,37]. In some cases, however, bursts of MHD activity develop, causing transient current jumps; these events are less frequent at low loop voltage. Increases in elongation, κ, were attempted to study its influence on the scenario, but RE beams were not observed for κ>1. The large dataset collected provides rich fodder for Fokker-Planck modeling [36].

Building on this scenario, explicit mitigation by magnetic control was investigated. An appropriately filtered plasma current signal is used to detect the onset of the current quench, upon which a new current reference is applied dynamically to induce a controlled shutdown. The controller actuates the Ohmic transformer primary through a novel double integrator control law. Termination of the RE beam over a range of total current values was demonstrated successfully [38]. The MHD events described above being clearly deleterious in this phase, future control developments, e.g. for ITER, should include criteria to minimize the loop voltage. An additional element should be an optimized radial control, since a slow drift of the RE beam towards the outer wall is observed during the final phase.

6. Real-time plasma control

The distributed digital control system of TCV is constantly evolving, with both hardware and software remaining state-of-the-art. A highly modular structure and the underlying reflective-memory paradigm permit the seamless addition of new CPU nodes, with or without attendant ADCs and DACs. Seven nodes are incorporated at present [39].

At the root of several control schemes is the real-time, sub-ms equilibrium reconstruction code RTLIUQE. In particular, this has been employed in the development of a generalized position and shape controller, based on boundary flux errors. The PI controller relies on a singular-value decomposition (SVD) approach to limit the controlled parameters to the subset that is most amenable to control. Weighting can be freely applied to constrain the main singular values to specific, physically meaningful quantities, such as vertical or radial position. An initial, time-invariant version was successfully tested on a variety of limited and diverted shapes, extending to negative-triangularity plasmas. The definitive, time-varying version for full plasma discharge control is in its final commissioning phase [39].

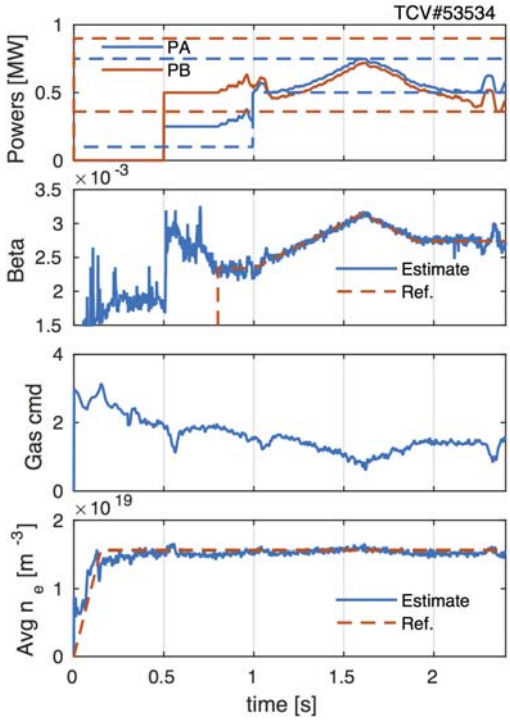

FIG. 9. TCV shot with simultaneous β and density control, using two ECRH sources (PA and PB). (Reproduced from [42].)

Experiments on NTM pre-emption and control with ECRH have continued, with the specific goal of providing input for modeling. The technique of sawtooth locking by ECRH, also indirectly related to NTM control, has been extended to higher β with NBH [6].

In a related development, a new real-time MHD mode analysis technique has been successfully tested. This employs a dedicated node to calculate the SVD of the fast magnetic-probe signals, the principal axes of which are then compared with markers computed from synthetic signals generated by a theoretical model of rotating modes [40].

The real-time control-oriented tokamak profile simulator RAPTOR [41] is at the core of a suite of physics-based models being developed for integrated-control and monitoring applications. It now incorporates models for NTMs, sawteeth, and plasma density evolution, plus parametrized models for heating sources [42]. Disruption prediction through the detection of anomalous sawtooth behavior has also been successfully demonstrated. The real-time estimation of the plasma state, particularly the density, pressure, and q profiles is provided by an Extended Kalman Filter (EKF). Various controllers for the plasma β and density and q profiles have been developed within this environment, using approaches such as adaptive control or model-based predictive control (MPC), and have been tested successfully on TCV (Fig. 9). Off-line applications of RAPTOR include the optimization of discharge ramp-up and ramp-down trajectories [42].

Controllers are generally developed in isolation and their integration into a generalized multi-controller environment is far from trivial, especially when they share (often scarce) actuators. A dedicated effort is underway to develop the know-how for the integration that will be necessary in a reactor. In the latest TCV campaign, the new shape controller, a predictive β controller, a model-based robust density controller [43], an MPC q profile controller, and an

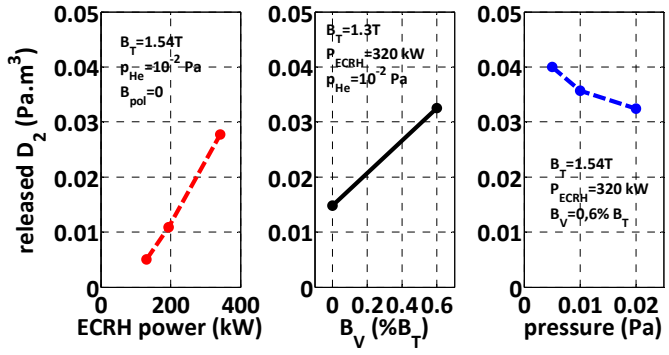

FIG. 10. Deuterium released as a function of ECRH power, vertical field, and He inlet pressure. (Reproduced from [44].)

NTM controller were demonstrated to operate simultaneously. More extensive and robust integration is a goal for future campaigns.

7. Impurities and wall conditioning

Effective techniques for impurity control, and particularly for the avoidance of heavy impurity accumulation from high-Z metal walls, need to be developed for ITER. The work performed on TCV in this area substitutes high-Z gases for metals. Initial investigations were performed in the latest campaign on the use of ECRH to prevent impurity accumulation and on the effect of poloidal asymmetries on impurity transport. Conversely, the (possibly beneficial) effect on confinement of impurity seeding has also been studied. Data analysis is ongoing and experiments will likely continue in the next campaign.

Wall conditioning with second-harmonic ECRH in He was explored in TCV in specific support of JT-60SA, which will have to rely on this technique because of technical constraints precluding more standard cleaning methods [44]. In addition to the main toroidal magnetic field, poloidal fields (a combination of radial and vertical fields) were applied and tuned to maximize the discharge homogeneity and wall coverage, the optimum field amplitude being ~0.1-0.6% of the toroidal field (Fig. 10). Further tuning was required on He gas injection and ECRH launcher orientation to minimize the time for breakdown and consequently the danger to the device components from stray radiation. The plasmas used had typical line-integrated densities ~1.5×10^{19} m^{-3} and electron temperatures ~20-40 eV. ECRH power was 90 to 480 kW, scaling to 1-5 MW for JT-60SA by wall surface area. Conditioning was demonstrated by a successful ensuing standard D2 plasma breakdown [44].

8. Conclusions and outlook

TCV is developing the physics basis for the evaluation of the viability of alternative divertor configurations for a DEMO reactor. Virtually all configurations proposed so far have been realized in TCV, and the associated exhaust physics, in attached and detached divertor conditions, is being studied with an extensive array of diagnostics. The remaining unanswered questions will be addressed by divertor upgrades, augmented by heating-power and diagnostic upgrades, to be completed by 2020.

New diagnostics and actuators have been deployed in pursuit of disruption mitigation and avoidance, and understanding and mitigation of runaway electrons.

The installation of a neutral beam injector has also made TCV a more direct contributor to ITER physics, with investigations progressing towards high-performance H-mode, exploring optimized confinement near the density limit, maximized pedestal height, and MHD instability avoidance. Advanced plasma control techniques including real-time physics-based modeling are a key element of this strategy.

Acknowledgments

This work has been carried out within the framework of the EUROfusion Consortium and has received funding from the Euratom research and training programme 2014-2018 under grant agreement number 633053. The views and opinions expressed herein do not necessarily reflect those of the European Commission. This work was supported in part by the Swiss National Science Foundation.

References

[1] HOFMANN, F., et al., Plasma Phys. Control. Fusion **36** (1994) B277.
[2] MEYER, H., et al, this conference, OV/P-12.
[3] KARPUSHOV, A.N., et al, submitted to Fus. Eng. and Design (2016).
[4] FASOLI, A., et al., this conference, FIP/P4-40.
[5] TOUSSAINT, M., et al, submitted to Fus. Eng. and Design (2016).
[6] DUVAL, B.P., et al, this conference, EX/P8-29.
[7] GEIGER, B., et al, this conference, EX/P8-30.
[8] TESTA, D., et al, Fusion Eng. and Design **96-97** (2015) 989.
[9] MARTIN, Y., et al, Proc. 43rd Conf. on Control. Fusion and Plasma Phys., Leuven, 2016, Europhys. Conf. Abstr. **40A** (2016) (P4.026).
[10] CHAPMAN, I.T., et al, this conference, EX/3-6.
[11] LAZZARO, E., et al, Nucl. Fusion **55** (2015) 093031.
[12] NOWAK, S., et al, this conference.
[13] CAMENEN, Y., et al., Nucl. Fusion **47** (2007) 510.
[14] POCHELON, A., et al, Plasma and Fusion Research **7** (2012) 2502148.
[15] DE VRIES, P.C., et al, this conference, EX/P6-41.
[16] REIMERDES, H., et al, this conference, EX/2-3.
[17] BOEDO, J.A., et al, Rev. Sci. Instrum. **80** (2009) 123506.
[18] VERHAEGH, K., et al, submitted to Nucl. Mater. Energy (2016).
[19] HARRISON, J.R., et al, submitted to Nucl. Mater. Energy (2016).
[20] THEILER, C., et al, submitted to Nucl. Fusion (2016).
[21] REIMERDES, H., et al., Plasma Phys. Control. Fusion **55** (2013) 124027.
[22] LABIT, B., et al, submitted to Nucl. Mater. Energy (2016).
[23] LUNT, T., et al., Plasma Phys. Control. Fusion **58** (2016) 045027.
[24] GALLO, A., et al, submitted to Nucl. Mater. Energy (2016).
[25] MAURIZIO, R., et al, Proc. 43rd Conf. on Control. Fusion and Plasma Phys., Leuven, 2016, Europhys. Conf. Abstr. **40A** (2016) (P4.027).
[26] FAITSCH, M., et al, Plasma Phys. Control. Fusion **57** (2015) 075005.
[27] NESPOLI, F., et al, J. Nucl. Mater. **463** (2015) 393.
[28] LABIT, B., et al, this conference, EX/P8-25.
[29] NESPOLI, F., et al, submitted to Nucl. Mater. Energy (2016).
[30] LABOMBARD, B., et al, Phys. Plasmas **8** (2001) 2107.
[31] VIANELLO, N., et al, this conference, EX/P8-26.
[32] KIRNEVA, N.A., et al, Proc. 43rd Conf. on Control. Fusion and Plasma Phys., Leuven, 2016, Europhys. Conf. Abstr. **40A** (2016) (P4.029).
[33] MARTIN, P., et al, this conference, EX/P6-23.
[34] ESPOSITO, B., et al, Nucl. Fusion **49** (2009) 065014.
[35] CODA, S., et al, Proceedings of Science **ECPD2015** (2015) 139.
[36] PAPP, G., et al, this conference, EX/9-4.
[37] PLYUSNIN, V.V., et al, this conference, EX/P6-33.
[38] ESPOSITO, B., et al, this conference, EX/P8-27.
[39] ANAND, H., et al, this conference, EX/P8-32.
[40] GALPERTI, C., et al, submitted to IEEE Trans. Nucl. Sci. (2016).
[41] FELICI, F., et al, Plasma Phys. Control. Fusion **54** (2012) 025002.
[42] FELICI, F., et al, this conference, EX/P8-33.
[43] BLANKEN, T.C., et al, Proc. 43rd Conf. on Control. Fusion and Plasma Phys., Leuven, 2016, Europhys. Conf. Abstr. **40A** (2016) (P4.031).
[44] DOUAI, D., et al, this conference, EX/P8-31.

Appendix: The TCV team

J. Ahn[2], R. Albanese[3], S. Alberti[1], E. Alessi[4], S. Allan[5], H. Anand[1], G. Anastassiou[6], Y. Andrèbe[1], C. Angioni[7], M. Ariola[8], M. Bernert[7], M. Beurskens[9], W. Bin[4], P. Blanchard[1], T. Blanken[10], J.A. Boedo[11], T. Bolzonella[12], F. Bouquey[2], F.H. Braunmüller[1], H. Bufferand[2], P. Buratti[13], G. Calabró[13], Y. Camenen[14], D. Carnevale[15], F. Carpanese[1], F. Causa[13], R. Cesario[13], I.T. Chapman[5], O. Chellai[1], D. Choi[1], C. Cianfarani[13], G. Ciraolo[2], J. Citrin[16], S. Coda[1], S. Costea[17], F. Crisanti[13], N. Cruz[18], A. Czarnecka[19], J. Decker[1], G. De Masi[12], G. De Tommasi[3], D. Douai[2], M. Dunne[7], B.P. Duval[1], T. Eich[7], S. Elmore[5], B. Esposito[13], M. Faitsch[7], A. Fasoli[1], N. Fedorczak[2], F. Felici[10], O. Février[2], O. Ficker[20], S. Fietz[7], M. Fontana[1], L. Frassinetti[21], I. Furno[1], S. Galeani[15], A. Gallo[2], C. Galperti[1], S. Garavaglia[4], I. Garrido[22], B. Geiger[7,9], E. Giovannozzi[13], M. Gobbin[12], T.P. Goodman[1], G. Gorini[23], M. Gospodarczyk[15], G. Granucci[4], J.P. Graves[1], R. Guirlet[2], A. Hakola[24], C. Ham[5], J. Harrison[5], J. Hawke[1], P. Hennequin[25], B. Hnat[26], D. Hogeweij[16], J.-Ph. Hogge[1], C. Honoré[25], C. Hopf[7], J. Horáček[20], Z. Huang[1], V. Igochine[7], P. Innocente[12], C. Ionita Schrittwieser[17], H. Isliker[27], R. Jacquier[1], A. Jardin[2], J. Kamleitner[1], A. Karpushov[1], D.L. Keeling[5], N. Kirneva[28,29], M. Kong[1], M. Koubiti[14], J. Kovacic[30], A. Krämer-Flecken[31], N. Krawczyk[19], O. Kudlacek[7,12], B. Labit[1], E. Lazzaro[4], H.B. Le[1], B. Lipschultz[32], X. Llobet[1], B. Lomanowski[33], V.P. Loschiavo[3], T. Lunt[7], P. Maget[2], B. Maljaars[10], A. Malygin[1], M. Maraschek[7], C. Marini[1], P. Martin[12], Y. Martin[1], S. Mastrostefano[8], R. Maurizio[1], M. Mavridis[27], D. Mazon[2], R. McAdams[5], R. McDermott[7], A. Merle[1], H. Meyer[5], F. Militello[5], I.G. Miron[34], P.A. Molina Cabrera[1], J.-M. Moret[1], A. Moro[4], D. Moulton[5], V. Naulin[35], F. Nespoli[1], A.H. Nielsen[35], M. Nocente[23], R. Nouailletas[2], S. Nowak[4], T. Odstrčil[7], G. Papp[7], R. Pápřok[20], A. Pau[36], G. Pautasso[7], V. Pericoli Ridolfini[8], P. Piovesan[12], C. Piron[12], T. Pisokas[27], L. Porte[1], M. Preynas[1], G. Ramogida[13], C. Rapson[7], J. Juul Rasmussen[35], M. Reich[7], H. Reimerdes[1], C. Reux[2], P. Ricci[1], D. Rittich[7], F. Riva[1], T. Robinson[5], S. Saarelma[5], F. Saint-Laurent[2], O. Sauter[1], R. Scannell[5], Ch. Schlatter[1], B. Schneider[17], P. Schneider[7], R. Schrittwieser[17], F. Sciortino[37], M. Sertoli[7], U. Sheikh[1], B. Sieglin[7], M. Silva[1], J. Sinha[1], C. Sozzi[4], M. Spolaore[12], T. Stange[9], T. Stoltzfus-Dueck[38], P. Tamain[2], A. Teplukhina[1], D. Testa[1], C. Theiler[1], A. Thornton[5], L. Tophøj[35], M.Q. Tran[1], C. Tsironis[6], C. Tsui[1], A. Uccello[4], S. Vartanian[2], G. Verdoolaege[39], K. Verhaegh[32], L. Vermare[25], N. Vianello[1,12], W.A.J. Vijvers[16], L. Vlahos[27], N.M.T. Vu[40], N. Walkden[5], T. Wauters[41], H. Weisen[1], M. Wischmeier[7], P. Zestanakis[6], M. Zuin[12]

[1]EPFL-SPC, Switzerland
[2]CEA, IRFM, France
[3]University of Napoli 'Federico II', Consorzio CREATE, Italy
[4]IFP-CNR, Italy
[5]CCFE, United Kingdom
[6]National Technical University of Athens, Greece
[7]IPP Garching, Germany
[8]University of Napoli Parthenope, Consorzio CREATE, Italy
[9]IPP Greifswald, Germany
[10]TUe, The Netherlands
[11]UCSD, United States
[12]Consorzio RFX, Italy
[13]ENEA, Italy
[14]CNRS/AMU, France
[15]University of Rome Tor Vergata, Italy
[16]DIFFER, The Netherlands

[17]Universität Innsbruck, Austria
[18]IST, Portugal
[19]Institute of plasma physics and laser microfusion, Poland
[20]Institute of plasma physics, Czech Republic
[21]Fusion plasma physics, EES-KTH, Sweden
[22]UPV/EHU, Spain
[23]University Milano-Bicocca, Italy
[24]VTT Technical Research Center, Finland
[25]LPP, France
[26]University of Oxford, United Kingdom
[27]Aristotle University of Thessaloniki, Greece
[28]RRC Kurchatov, Russian Federation
[29]NRNU MEPhI, Russian Federation
[30]Jožef Stefan Institute, Slovenia
[31]Forschungszentrum Jülich, Germany
[32]University of York, United Kingdom
[33]Durham University, United Kingdom
[34]National Institute for Laser, Plasma and Radiation Physics, Romania
[35]Technical University of Denmark, Denmark
[36]University of Cagliari, Italy
[37]Plasma Science and Fusion Center, MIT, United States
[38]Princeton University, US
[39]Ghent University, Belgium
[40]LCIS, Grenoble Institute of Technology, France
[41]Koninklijke Militaire School, Belgium